

https://dspace.org/

Surface dynamics on Jeffrey nanofluid flow with Coriolis effect and variable Darcy regime

Y Tijani; M Akolade; Olumuyiwa Otegbeye; A Yusuf

https://hdl.handle.net/10539/41123
WOS

Downloaded from a DSpace repository. https://dspace.org/

Check for updates

Received: 10 March 2023 | Revised: 27 June 2023 | Accepted: 22 August 2023

DOI: 10.1002/zamm.202300217

ORIGINAL PAPER

Surface dynamics on Jeffrey nanofluid flow with Coriolis effect and variable Darcy regime

Yusuf O. Tijani[1] | **Mojeed T. Akolade**[2] | **Olumuyiwa Otegbeye**[3] | **Abdulhakeem Yusuf**[4]

[1]Department of Mathematics and Applied Mathematics, Nelson Mandela University, Port-Elizabeth, South Africa

[2]Department of Mathematics, Faculty of Computing and Applied Sciences, Thomas Adewumi University, Oko, Kwara, Nigeria

[3]School of Computer Science and Applied Mathematics, University of Witwatersrand, Johannesburg, South Africa

[4]Department of Mathematics, Federal University of Technology Minna, Minna, Nigeria

Correspondence
Yusuf O. Tijani, Department of Mathematics and Applied Mathematics, Nelson Mandela University, Port-Elizabeth 6031, South Africa.
Email: olodyusuf@gmail.com

Stretching and shrinking application ranges from aerodynamic extrusion of plastic sheets, biological implants, condensation of metallic plates to the design of musical instruments. To emphasize the need for proper fluid flow in the mammalian system, the phenomenon of stretching or shrinking suppresses muscle strains and cramps, and also prevents stroke and heart disease. For further insight into the dynamics of blood with Prandtl number of 21.0 in a rotating system, the present study theoretically investigates the flow of a Jeffrey fluid induced with gold nanoparticles over a rotating sheet. The homogenization of the gold nanoparticle with the base fluid is due to the Tiwari-Das approach. To investigate the flow profiles and dynamics of the sheet, the spectral local linearization method (SLLM) is used to obtain approximate solutions to the resulting system of nonlinear differential equations. The results obtained using the SLLM are validated by taking the limiting case and comparing against published literature results. The obtained results suggest that the velocity of the nanofluid and the heat transfer rate on the stretching and shrinking sheets exhibit an opposing behaviour. A blood sample with gold nanoparticles is advised for a reduced skin friction effect in the stretching sheet but a more significant drag force in the shrinking sheet than in the base fluid. For a unit value of the rotating parameter, the skin drag force reduces by 36% for the primary skin drag force and 57% for the secondary skin drag force.

1 | INTRODUCTION

Theoretically, fluid particles will move in response to a shear force, resulting in a permanent change to their relative positions, even after the force has been removed [1]. Rotating flow refers to the movement of fluids observed from a non-inertial frame of reference. The dynamics of fluid flow within a moving system have always captivated researchers throughout history, particularly in phenomena like hurricanes, tornadoes, and cyclones. This phenomenon has led to the design of many industrial and engineering applications. A typical example is the paddling of a ship, the design of aircraft wings in shedding vortices and pistons design in engines [1]. Research attention has been spotlighted on rotating fluid due to its immersive application. Among the numerous studies are the works of Tokis [2], Nanousis [3], and Abbas *et al.* [4] on unsteady magnetohydrodynamics (MHD) free convection flows in a rotating system, Shafique *et al.* [5] analyzed binary chemical reaction and activation energy for Maxwell fluid rheology subjecting the working system to the Coriolis effect among others.

 © 2023 Wiley-VCH GmbH.

In research, the significance of the flow of non-Newtonian fluid, which is the direct opposite of Newtonian fluid in the presence of heat transfer, can never be overemphasized due to its wide application in food processing, power engineering, petroleum production and other industrial processes. Fluids such as cosmetics, taffy, vanilla, blood, saliva, and synovial all exhibit non-Newtonian behavior. The modeling of heat transfer of nanofluids with low-volume fraction of nanoparticles in a Newtonian base fluid can be done using the Newtonian model; in some cases, the fluids with Newtonian base exhibit the behavior of non-Newtonian fluids [6–8]. The study of the rheological property of polycarbonate, which contains 0.5–15 weight per cent, was carried out by Pötschke *et al.* [9]. They found that over the threshold of two weight per cent, nanotubes exhibited non-Newtonian behavior. Phuoc *et al.* [10] experimented with multi-walled carbon nanotube nanofluids' viscosity and reported a 20% decrease was observed. They further reported that increased viscosity leads to non-Newtonian shear thinning fluid. The compositions of these fluids give rise to the development of more informative and higher-order model equations over the Navier-Stoke equation. Jeffrey fluid is a type of non-Newtonian fluid that exhibits viscoelastic behavior. The stress and strain rates in Jeffrey fluid are not linearly proportional to each other as they are in Newtonian fluids, but rather depend on the fluid's viscosity, elasticity, and the rate of deformation. One of the important features of Jeffrey fluids is their sensitivity to shear rate. At low shear rates, the fluid behaves as if it has a high viscosity, while at high shear rates, it behaves as if it has a low viscosity. Jeffrey fluids have many practical applications, including in the manufacturing of paints, printing inks, and cosmetic products. It is used in studying bolus movement through the oesophagus, movement of chyme in the small intestine and aqueous polyacrylamide solution. They are also used in the design of artificial joint fluids and for modeling biological fluids such as blood and mucus. The Jeffrey model has significantly been employed in the model of blood flow. In physiology, MHD has several applications ranging from magnetic resonance imaging, magnetic particles used in drug transferals, blood generated in the presence of haemoglobin molecules and magnetic devices, see Hayat *et al.* [11] . The Jeffrey model was used by Rao *et al.* [12] to investigate the effects of the Hartman number on the considered distributions; they found that the Hartman number has a similar effect on the distribution profiles and that the Deborah number causes the fluid temperature and concentration profiles to drop significantly. In a revised model of Jeffrey fluid by Hayat *et al.* [13], the heat transfer response over a non-Isothermal wedge was expunged. They reported that enhancing the ratio of relaxation to retardation times accelerates the fluid velocity while the temperature is decelerated. In a related study by Hussain *et al.* [14], the influence of thermal radiation on magnetized stretching sheets is explored. Hayat and Mustafa [15] analyzed the time-dependent mixed convective flow of the Jeffrey fluid using the homotopy analysis method and reported the effects of thermal radiation on the distributions. A study on unsteady MHD oscillatory flow of the Jeffrey fluid subject to chemical reaction effect was carried out by Idowu *et al.* [16]. At the same time, the impact of heat and mass transfer was recorded. A ramped wall temperature was applied to a free convective Jeffrey fluid flow by Zin *et al.* [17]. It was demonstrated that the impact of radiation is very pronounced. Using a permeable plate with fluid remover and depositor, Zeeshan and Majeed [18] studied the influence of magnetic dipoles on forced Jeffrey fluid flow. More works on the significance of the Jeffrey model can be found in refs. [19–21]. In a related study, Li *et al.* [22] examine the unsteady flow of viscous liquid subjected to an induced magnetic field where the flow is control via uniform suction. They reported that the induced magnetic field is augmented as a result of improvement in suction variable. Hayat *et al.* [23] presented an analytical solution of axisymmetric steady boundary layer flow over a continuous stretching cylinder with magnetic field. For third grade fluid, velocity profile is found to be higher compared to Newtonian and second grade fluid in the absence/presence of MHD. Hayat *et al.* [24] study MHD flow of third grade fluid in two parallel permeable disks with heat transfer. Further study in this direction can be found in refs. [25, 26].

In general, the attraction of fluid toward the slot (origin) is what distinguishes shrinking surfaces from stretching surfaces. It is important to note that the flow of a Jeffrey fluid over shrinking and stretching surfaces is crucial to many engineering applications such as contracting films, hot rolling, and metal spinning. It was examined by Hamid *et al.* [27] how Ohmic heating and viscous dissipation in Williamson fluid flow influenced by expanding and compressing sheets in the context of time-dependent magnetic fields. The effects of thermal radiation on MHD flow past a shrinking and stretching sheet were considered by Yasin *et al.* [28], and the dual solutions were reported. Investigation of the influence of Newtonian heating on MHD micropolar nano liquid on both stretching and the shrinking sheet was carried out by Gangadhar *et al.* [29]. They reported the existence of multiple solutions for the moving sheets. Several researchers, such as refs. [8, 30, 31], have all conducted studies on stretching/shrinking sheets.

Jeffrey fluid is one of the most transparent and fascinating non-Newtonian fluids. Due to the viscoelastic behavior of the fluid, it has a wide-ranging scope of application in many fields of science and engineering. In light of the literature above, the novelty of this study lies in identifying the impact of surface dynamics (stretching and shrinking) on the rheological model of Jeffrey fluid, subject to the Coriolis effect, magnetic response, fluid relaxation time, and observing the thermal performance of blood via the injection of gold (Au) nanoparticles in variable porous media. To conduct the study,

15214001, 2024, 2, Downloaded from https://onlinelibrary.wiley.com/doi/10.1002/zamm.202300217 by University Of Witwatersrand, Wiley Online Library on [20/08/2024]. See the Terms and Conditions (https://onlinelibrary.wiley.com/terms-and-conditions) on Wiley Online Library for rules of use; OA articles are governed by the applicable Creative Commons License



FIGURE 1 Paper setup flow chart.

the spectral local linearization method (SLLM), introduced by Motsa [32], is used to solve the resulting system of nonlinear differential equations. The findings of this study are highly applicable to the medical and engineering communities, particularly in relation to the centrifugation of blood.

2 | ORGANIZATION OF THE PAPER

The paper setup is as follows. Section 3 contains the model formulation analysis resulting in the dimensional governing flow equations, the nanofluid physical properties/relation and the similarity technique. The mathematical model flowchart is given in Figure 1. In Section 4 we present the convergence analysis, numerical validation, and numerical solution via the SLLM implemented on matrix laboratory (MATLAB). The importance of each emerging flow parameter

15214001, 2024, 2, Downloaded from https://onlinelibrary.wiley.com/doi/10.1002/zamm.202300217 by University Of Witwatersrand, Wiley Online Library on [20/08/2024]. See the Terms and Conditions (https://onlinelibrary.wiley.com/terms-and-conditions) on Wiley Online Library for rules of use; OA articles are governed by the applicable Creative Commons License

as well as the surface dynamics is discussed in Section 5. Finally, the results and significance of the present study are elaborated on in Section 6.

3 | MODEL FORMULATION

The three dimensional rotating flow of a nanofluid over a sheet with the existence of Coriolis force and magnetic effect is the concern of this model.

$$\nabla \cdot \vec{q} = 0. \tag{1}$$

$$\rho\left(\frac{D\vec{q}}{Dt} + 2\vec{\Omega}\times\vec{q} + \vec{\Omega}\times(\vec{\Omega}\times\vec{r})\right) = -\nabla p + \nabla\cdot\tau + \vec{J}\times\vec{B} - \mu\frac{\vec{q}}{K}. \tag{2}$$

$$\rho c_p\left(\frac{DT}{Dt}\right) = \kappa\nabla^2 T - \nabla q_r' - Q_*\Delta T. \tag{3}$$

τ is the constitutive Cauchy stress relation for Jeffrey fluid and it is given by

$$\tau = -pI + \frac{\mu}{1+\Gamma_1}\left[(\nabla\vec{q} + (\nabla\vec{q})^j) + \Gamma_2\left(\frac{\partial(\nabla\vec{q} + (\nabla\vec{q})^j)}{\partial t} + \vec{q}\cdot\nabla\right)(\nabla\vec{q} + (\nabla\vec{q})^j)\right], \tag{4}$$

where the superscript j represents the transpose of $\nabla\vec{q}$, Γ_1 and Γ_2 are the Jeffrey fluid parameters. $\vec{q}$ is the fluid velocity vector relative to the moving coordinate system and I represents the identity tensor. The second term on the left side of Equation (2) is the Coriolis force, and the third term on the left side of Equation (2) is the centrifugal force, see ref. [33]. These terms arise due to the rotation of the coordinate system and thus are not really true forces. The first term on the right hand side stands for the pressure gradient, while the second, third and fourth represent the fluid rheology, magnetic force and porous terms respectively. The radiative term is represented in Equation (3) by the second term on the right hand side and heat source is represented by the third term. An incompressible nanofluid, with no chemical reactions is assumed to be a two component mixture. The surface dynamics aligns on-point with the plane $z = 0$ and $u_w = ax$. The fluid is rotating with a constant angular velocity λ about the z-axis. The surface dynamics distance x is also rotating with the fluid. The Coriolis force contributes to the three-dimensionality of the flow in terms of spatial variables. The magnetic field $B = (0, B_0, 0)$ is imposed in the z-direction. The flow is electrically conducting. Electrical energy is added to and extracted from the fluid in this case through the magnetic term. Other body forces like gravitational force, pressure gradient (∇p) and Darcy-Forchemer effect are not factored in this model. In addition, the flow is of steady kind. Temperature of the sheet is represented by T_w which is smaller compared to the ambient temperature of the sheet indicated by T_∞ see Figure 2. The flow in regard to conservation equations are similar to those in Wang [34] and Iqbal *et al.* [33] given as

$$\frac{\partial u}{\partial x} + \frac{\partial w}{\partial z} = -\frac{\partial v}{\partial y}. \tag{5}$$

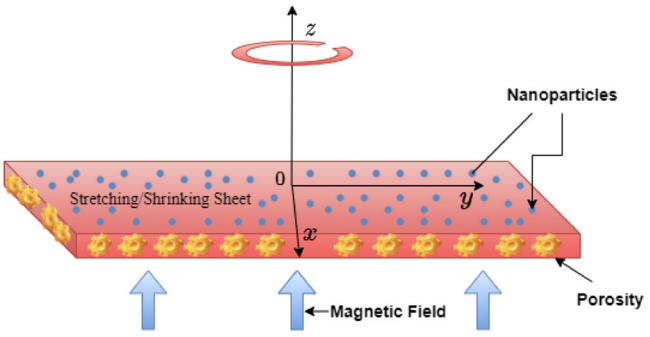


FIGURE 2 Flow configuration.

15214001, 2024, 2, Downloaded from https://onlinelibrary.wiley.com/doi/10.1002/zamm.202300217 by University Of Witwatersrand, Wiley Online Library on [20/08/2024]. See the Terms and Conditions (https://onlinelibrary.wiley.com/terms-and-conditions) on Wiley Online Library for rules of use; OA articles are governed by the applicable Creative Commons License

$$u\frac{\partial u}{\partial x}+\upsilon\frac{\partial u}{\partial y}+w\frac{\partial u}{\partial z}-2\lambda\upsilon=\frac{1}{1+\Gamma_1}\frac{\mu_{nf}}{\rho_{nf}}\left(\frac{\partial^2 u}{\partial z^2}\right)-\frac{\sigma_{nf}B^2u}{\rho_{nf}}-\frac{\mu_{nf}}{\rho_{nf}}\frac{u}{K(z)}$$
$$+\frac{\Gamma_2}{1+\Gamma_1}\frac{\mu_{nf}}{\rho_{nf}}\left(u\frac{\partial^3 u}{\partial x\partial z^2}+\upsilon\frac{\partial^3 u}{\partial y\partial z^2}+w\frac{\partial^3 u}{\partial z^3}+\frac{\partial u}{\partial z}\frac{\partial^2 u}{\partial x\partial z}+\frac{\partial \upsilon}{\partial z}\frac{\partial^2 u}{\partial y\partial z}+\frac{\partial w}{\partial z}\frac{\partial^2 u}{\partial z^2}\right). \tag{6}$$

$$u\frac{\partial \upsilon}{\partial x}+\upsilon\frac{\partial \upsilon}{\partial y}+w\frac{\partial \upsilon}{\partial z}+2\lambda u=\frac{1}{1+\Gamma_1}\frac{\mu_{nf}}{\rho_{nf}}\left(\frac{\partial^2 \upsilon}{\partial z^2}\right)-\frac{\sigma_{nf}B^2\upsilon}{\rho_{nf}}-\frac{\mu_{nf}}{\rho_{nf}}\frac{\upsilon}{K(z)}$$
$$+\frac{\Gamma_2}{1+\Gamma_1}\frac{\mu_{nf}}{\rho_{nf}}\left(u\frac{\partial^3 \upsilon}{\partial x\partial z^2}+\upsilon\frac{\partial^3 \upsilon}{\partial y\partial z^2}+w\frac{\partial^3 \upsilon}{\partial z^3}+\frac{\partial u}{\partial z}\frac{\partial^2 \upsilon}{\partial x\partial z}+\frac{\partial \upsilon}{\partial z}\frac{\partial^2 \upsilon}{\partial y\partial z}+\frac{\partial w}{\partial z}\frac{\partial^2 \upsilon}{\partial z^2}\right). \tag{7}$$

$$u\frac{\partial T}{\partial x}+\upsilon\frac{\partial T}{\partial y}+w\frac{\partial T}{\partial z}=-\frac{1}{(\rho c_p)_{nf}}\frac{\partial q_r}{\partial z}+\frac{\kappa_{nf}}{(\rho c_p)_{nf}}\left(\frac{\partial^2 T}{\partial z^2}\right)-\frac{Q_o}{(\rho c_p)_{nf}}(T-T_\infty). \tag{8}$$

The appropriate boundary conditions are

$$\left.\begin{aligned} &u=\xi u_w(x),\quad \upsilon=0,\quad w=0,\quad T=T_w\quad \text{at}\quad =0,\\ &u\to 0,\quad \upsilon\to 0,\quad T\to T_\infty,\quad \text{as}\quad z\to\infty. \end{aligned}\right\} \tag{9}$$

Here, u and υ are the velocity components in x and y axes respectively, T represent the temperature of the fluid, ρ is the fluid density, c_p stands for the specific heat capacity of the fluid, ν is the kinematic viscosity, K stands for the permeability parameter, Γ_1 is the ratio of $\frac{\text{relaxation times}}{\text{retardation times}}$, $u_w(x)$ is the mainstream velocity, k is the thermal conductivity and ξ is the stretching/shrinking parameter. The linear radiative heat flux resulting from the Rosseland approximation is defined as, see Akolade and Tijani [35]

$$q_r=-\frac{4\sigma^*}{3k_1}\frac{\partial T^4}{\partial z}=-\frac{16\sigma^*}{3k_1}\left[T_\infty^3\frac{\partial T}{\partial z}\right]. \tag{10}$$

q_r stands for the radiative term, k_1 represents the mean absorption coefficient and σ^* is the Stefan–Boltzman constant. It is worth mentioning that Equation (10) will be substituted into Equation (8) to obtain appropriate temperature flow equation. Following [36–39], the variable Darcy model defined in Equation (11) is incorporated into the momentum equations (6) and (7),

$$K(z)=\frac{m_p^2\,\lambda(z)^3}{175(1-\lambda(z))^2};\qquad \text{Such that}\qquad \lambda(z)=\xi_0\left(1+\xi_1 e^{-\frac{\xi_2 z}{m_p}}\right), \tag{11}$$

where ξ_1 and ξ_2 are the empirical constants subject to porous particle diameter, ξ_0 represent the ambient porosity and m_p is the particle diameter. The experimental value of the embedding parameters ξ_0, ξ_1, ξ_2, and Pr are used (fixed value) for simulation.

3.1 | Thermophysical properties of the nanofluid

The mathematical expression of the nanofluid and the base fluid properties (i.e., viscosity, volumetric heat capacity, density and thermal conductivity) are given [42, 43] for fluid viscosity as $\Lambda_1=\frac{\mu_{nf}}{\mu_f}=\frac{1}{(1-\phi)^{2.5}}$, specific heat capacity as $(\rho c_p)_{nf}=(1-\phi)(\rho c_p)_f+\phi(\rho c_p)_s$, fluid density as $\rho_{nf}=(1-\phi)\rho_f+\phi\rho_s$, thermal conductivity as $\frac{\kappa_{nf}}{\kappa_f}=\frac{(\kappa_s+2\kappa_f)-2\phi(\kappa_f-\kappa_s)}{(\kappa_s+2\kappa_f)+2\phi(\kappa_f-\kappa_s)}$ and electrical conductivity as $\frac{\sigma_{nf}}{\sigma_f}=\left[1+\frac{3(\frac{\sigma_s}{\sigma_f}-1)\phi}{(\frac{\sigma_s}{\sigma_f}+2)-(\frac{\sigma_s}{\sigma_f}-1)\phi}\right]$, where the subscripts f and s represent the base fluid and nanoparticle respectively. ϕ stands for nanoparticle volume fraction. Table2 shows the numerical value of the thermophysical properties of the base fluid (blood) and the nanoparticle.

15214001, 2024, 2, Downloaded from https://onlinelibrary.wiley.com/doi/10.1002/zamm.202300217 by University Of Witwatersrand, Wiley Online Library on [20/08/2024]. See the Terms and Conditions (https://onlinelibrary.wiley.com/terms-and-conditions) on Wiley Online Library for rules of use; OA articles are governed by the applicable Creative Commons License

TABLE 1 Experimental value of the thermophysical parameter in accordance with blood as the based fluid [36–41].

Parameter	ξ_0	ξ_1	ξ_2	D_a	Pr	M	Ω	ϕ	R	β	Q	Γ_1
Value	2.5	0.98	1.0	10.0	21	2.0	1.0	0.02	2.0	0.01	0.0001	2.0

TABLE 2 Thermophysical features of nanoparticles and base fluid, see refs. [44, 45].

	ρ [kg·m^{-3}]	k [W·m^{-1}·K^{-1}]	C_p [J·kg^{-1}·K^{-1}]	σ [S·m^{-1}]
Blood	1063	0.492	3594	0.667
Au	19320	314	129	4.52×10^7

3.2 | Similarity transformation

The appropriate similarity transformation approach for the mathematical model given in Equations (5)–(8) is given as, Iqbal *et al.* [33]

$$u = axf'(\eta), \quad \eta = \sqrt{\frac{a}{\nu}}z, \quad v = axg(\eta), \quad \theta = \frac{T - T_\infty}{T_w - T_\infty}, \quad w = -\sqrt{a\nu}f(\eta). \tag{12}$$

Implementing this transformation on the model Equations (5), (6), (8) and boundary conditions in Equation (9), we obtain the following differential equations given by

$$\begin{aligned} &f''' + \beta\left(f''^2 - ff^{iv}\right) - \frac{\Lambda_2}{\Lambda_1}(1+\Gamma_1)(f'^2 - ff'') \\ &+ 2\frac{\Lambda_2}{\Lambda_1}\Omega(1+\Gamma_1)g - \frac{\Lambda_3}{\Lambda_1}M(1+\Gamma_1)f' - \frac{(1+\Gamma_1)}{D_a}\frac{175\left[1-\xi_0\left(1+\xi_1 e^{-\frac{\xi_2}{\sqrt{D_a}}\eta}\right)\right]^2}{\xi_0^3\left(1+\xi_1 e^{-\frac{\xi_2}{\sqrt{D_a}}\eta}\right)^3}f' = 0. \end{aligned} \tag{13}$$

$$\begin{aligned} &g'' + \beta\left(f''g' - fg'''\right) - \frac{\Lambda_2}{\Lambda_1}(1+\Gamma_1)(f'g - fg') \\ &- 2\frac{\Lambda_2}{\Lambda_1}\Omega(1+\Gamma_1)f' - \frac{\Lambda_3}{\Lambda_1}M(1+\Gamma_1)g - \frac{(1+\Gamma_1)}{D_a}\frac{175\left[1-\xi_0\left(1+\xi_1 e^{-\frac{\xi_2}{\sqrt{D_a}}\eta}\right)\right]^2}{\xi_0^3\left(1+\xi_1 e^{-\frac{\xi_2}{\sqrt{D_a}}\eta}\right)^3}g = 0. \end{aligned} \tag{14}$$

$$\left(\Lambda_5 + \frac{4}{3}R\right)\theta'' + \Lambda_4 Prf\theta' - PrQ\theta = 0. \tag{15}$$

Here, $\Lambda_2 = \frac{\rho_{nf}}{\rho_f}, \Lambda_3 = \frac{\sigma_{nf}}{\sigma_f}, \Lambda_4 = \frac{(\rho c_p)_{nf}}{(\rho c_p)_f}, \Lambda_5 = \frac{\kappa_{nf}}{\kappa_f}$ are the nanofluid parameters. $\beta = \Gamma_2 a$ stands for retardation time constant, $\Omega = \frac{\lambda}{a}$ stands for Eckman number, $M = \frac{\sigma_f B^2}{a\rho_f}$ is magnetic parameter, $D_a = \frac{\nu_f}{am_p^2}$ is the dimensionless porosity parameter, $Pr = \frac{(\rho c_p)_f \nu_f}{\kappa_f}$ is the Prandtl number, $Q = \frac{Q_o}{a(\rho c_p)_f}$ is the heat source parameter and $R = \frac{4\sigma^* T_\infty^3}{k_1 \kappa_f}$ stands for radiation parameter. Note that the primary and secondary velocity are order four and three differential equations respectively. To accommodate this condition for solvability purpose, an appropriate boundary condition is given as [33]

$$\frac{\partial u}{\partial z} \to 0 \text{ and } \frac{\partial v}{\partial z} \to 0 \text{ as } \eta \to \infty. \tag{16}$$

15214001, 2024, 2, Downloaded from https://onlinelibrary.wiley.com/doi/10.1002/zamm.202300217 by University Of Witwatersrand, Wiley Online Library on [20/08/2024]. See the Terms and Conditions (https://onlinelibrary.wiley.com/terms-and-conditions) on Wiley Online Library for rules of use; OA articles are governed by the applicable Creative Commons License

Thus, the dimensionless boundary conditions becomes

$$\begin{aligned} &f'(\eta)=\xi, \quad f(\eta)=0, \quad g(\eta)=0, \quad \theta(\eta)=1, \quad \text{at} \quad \eta=0, \\ &f'(\eta)\to 0, \quad f''(\eta)=0, \quad g(\eta)\to 0, \quad g'(\eta)\to 0, \quad \theta(\eta)\to 0, \quad \text{as} \quad \eta\to\infty. \end{aligned} \tag{17}$$

Where $\xi=0$ implies non-moving sheet, $\xi>0$ means stretching sheet and $\xi<0$ denotes shrinking sheet.

The engineering physical parameters of interest, that is, the surface drag (skin friction) coefficient and Nusselt number, are defined as follows

$$C_{fx}=\frac{\tau_{wx}}{\rho_f u^2}, \quad C_{fy}=\frac{\tau_{wy}}{\rho_f v^2}, \quad Nu_x=\frac{xq_w}{\kappa_f(T_w-T_\infty)}, \tag{18}$$

$$\begin{aligned} \tau_{xz}&=\frac{\mu_{nf}}{1+\Gamma_1}\left[\frac{\partial u}{\partial z}+\Gamma_2\left(u\frac{\partial^2 u}{\partial x\partial z}+v\frac{\partial^2 u}{\partial y\partial z}+w\frac{\partial^2 u}{\partial z^2}+\frac{\partial u}{\partial x}\frac{\partial u}{\partial z}+\frac{\partial u}{\partial y}\frac{\partial v}{\partial z}+\frac{\partial u}{\partial z}\frac{\partial w}{\partial z}\right)\right]\Big|_{z=0}, \\ \tau_{yz}&=\frac{\mu_{nf}}{1+\Gamma_1}\left[\frac{\partial v}{\partial z}+\Gamma_2\left(u\frac{\partial^2 v}{\partial x\partial z}+v\frac{\partial^2 v}{\partial y\partial z}+w\frac{\partial^2 v}{\partial z^2}+\frac{\partial v}{\partial x}\frac{\partial u}{\partial z}+\frac{\partial v}{\partial y}\frac{\partial v}{\partial z}+\frac{\partial v}{\partial z}\frac{\partial w}{\partial z}\right)\right]\Big|_{z=0}, q_w=-\kappa_f\frac{\partial T}{\partial y}\Big|_{y=0}-q_r. \end{aligned} \tag{19}$$

In dimensionless form, Equation (18) with Equation (19) becomes

$$\begin{aligned} Re_x^{\frac{1}{2}}C_{fx}&=\frac{\Lambda_1}{\Lambda_2}\frac{1}{1+\Gamma_1}\left[f''(0)+\beta\left(f'(0)f''(0)-f(0)f'''(0)\right)\right], \\ Re_x^{\frac{1}{2}}C_{fy}&=\frac{\Lambda_1}{\Lambda_2}\frac{1}{1+\Gamma_1}\left[g'(0)+\beta\left(g(0)f''(0)-f(0)g''(0)\right)\right], \quad Re_x^{-\frac{1}{2}}Nu_x=-\left(\Lambda_5+\frac{4}{3}R\right)\theta'(0), \end{aligned} \tag{20}$$

where $Re_x=\frac{u_w^2}{a\nu}$ is the Reynolds number.

4 | SPECTRAL LOCAL LINEARIZATION METHOD

In this section, we discuss the implementation of the SLLM on the coupled system of non-linear differential equations (13)–(15). The SLLM involves the use of Taylor series expansion on univariate functions and its derivatives to first order. By performing univariate expansions on the nonlinear terms, the coupled system is effectively decoupled and leads to a decoupled system of linear differential equations where updated solutions from previous equations are used in subsequent equations. The linear equations are further discretized by applying a linear transformation and using Chebyshev-Gauss-Lobatto collocation points and solved with the Chebyshev spectral collocation method. We refer the reader to the studies by Motsa [46] and Otegbeye *et al.* [47] for full description of the SLLM. To apply the SLLM on [13–15], linearization is performed and we obtain;

$$\zeta_{1,a}f^{iv}_{(a+1)}+\zeta_{2,a}f'''_{(a+1)}+\zeta_{3,a}f''_{(a+1)}+\zeta_{4,a}f'_{(a+1)}+\zeta_{5,a}f_{(a+1)}=R_{f_1}. \tag{21}$$

$$\zeta_{6,a}g'''_{(a+1)}+\zeta_{7,a}g''_{(a+1)}+\zeta_{8,a}g'_{(a+1)}+\zeta_{9,a}g_{(a+1)}=R_{g_1}. \tag{22}$$

$$\zeta_{10,a}\theta''_{(a+1)}+\zeta_{11,a}\theta'_{(a+1)}+\zeta_{12,a}\theta_{(a+1)}=R_{\theta_1}. \tag{23}$$

as well as appropriate boundary conditions

$$\begin{aligned} f'_{(a+1)}&=\xi, f_{(a+1)}=0, g_{(a+1)}=0, \theta_{(a+1)}=1, \text{ for } \eta=0, \\ f'_{(a+1)}&=0, f''_{(a+1)}\to 0, g_{(a+1)}=0, g'_{(a+1)}\to 0, \theta_{(a+1)}=0, \text{ as } \eta\to\infty. \end{aligned} \tag{24}$$

15214001, 2024, 2, Downloaded from https://onlinelibrary.wiley.com/doi/10.1002/zamm.202300217 by University Of Witwatersrand, Wiley Online Library on [20/08/2024]. See the Terms and Conditions (https://onlinelibrary.wiley.com/terms-and-conditions) on Wiley Online Library for rules of use; OA articles are governed by the applicable Creative Commons License

and the variable (coefficient) outlined as

$$\begin{cases} \zeta_{1,a} = \beta f, \zeta_{2,a} = 1, \zeta_{3,a} = 2\beta f'' + \frac{\Lambda_2}{\Lambda_1}(1+\Gamma_1)f, \\ \zeta_{4,a} = -2\frac{\Lambda_2}{\Lambda_1}(1+\Gamma_1)f' - \frac{\Lambda_3}{\Lambda_1}M(1+\Gamma_1) - \frac{(1+\Gamma_1)}{D_a}\frac{175\left[1-\xi_0\left(1+\xi_1 e^{-\frac{\xi_2}{\sqrt{D_a}}\eta}\right)\right]^2}{\xi_0^3\left(1+\xi_1 e^{-\frac{\xi_2}{\sqrt{D_a}}\eta}\right)^3}, \zeta_{5,a} = -\beta f^{iv} + \frac{\Lambda_2}{\Lambda_1}M(1+\Gamma_1)f'' \\ \zeta_{6,a} = -\beta f, \Omega_{7,a} = 1.0, \zeta_{8,a} = \beta f'' + \frac{\Lambda_3}{\Lambda_1}M(1+\Gamma_1)f'' \frac{2}{3}\frac{\Lambda_2}{\Lambda_4}f, \\ \zeta_{9,a} = -\frac{\Lambda_2}{\Lambda_1}(1+\Gamma_1)f' - \frac{\Lambda_3}{\Lambda_1}M(1+\Gamma_1) - \frac{(1+\Gamma_1)}{D_a}\frac{175\left[1-\xi_0\left(1+\xi_1 e^{-\frac{\xi_2}{\sqrt{D_a}}\eta}\right)\right]^2}{\xi_0^3\left(1+\xi_1 e^{-\frac{\xi_2}{\sqrt{D_a}}\eta}\right)^3}, \zeta_{10,a} = \Lambda_5 + \frac{4}{3}R, \zeta_{(11,a)} = \Lambda_4 Prf, \\ \zeta_{(12,a)} = -PrQ. \end{cases} \tag{25}$$

and residuals

$$\begin{cases} R_{f_1} = \zeta_{1,a} f^{iv}_{(a)} + \zeta_{2,a} f'''_{(a)} + \zeta_{3,a} f''_{(a)} + \zeta_{4,a} f'_{(a)} + \zeta_{5,a} f_{(a)} - L_1 \\ R_{g_1} = \Omega_{6,a} g'''_{(a)} + \Omega_{7,a} g''_{(a)} + \Omega_{8,a} g'_{(a)} + \Omega_{9,a} g_{(a)} - L_2 \\ R_{\theta_1} = \zeta_{10,a} \theta''_{(a)} + \zeta_{11,a} \theta''_{(a)} + \zeta_{12,a} \theta''_{(a)} - L_3 \end{cases} \tag{26}$$

where L_1, L_2 and L_3 represent Equations (13), (14) and (15) respectively. The first step in our iterative scheme is to select a suitable guess function, which can be define as follows;

$$f_{1(a)} = \xi - \xi e^{-\eta}, \quad g_{1(a)} = 0 \text{ and } \theta_{1(a)} = e^{-\eta}. \tag{27}$$

For brevity, the description of the linear transformation, discretization, and solution method is given in studies conducted in refs. [35, 46, 48–50]. To briefly describe the simulation process, we provide the algorithm for the SLLM under the assumption that the well known "cheb" function given by Trefethen [51] is utilized.

Start
Define grid points
Obtain the differentiation matrix and discretization points using the cheb **function**
Truncate the semi-finite domain using a finite value
Transform the semi-finite domain into a finite domain [−1,1]
Scale the differentiation matrix
Define parameters
Define initial guess/solution
For r **in** iterations
    create matrices by replicating the initial guesses
    define the functions and derivatives
    define matrices
    impose boundary conditions
    define the known vector (RHS)
    impose conditions on the known vector
    solve to obtain the unknown vector
    update the solution
    repeat the steps above **for** the subsequent equations
End

15214001, 2024, 2, Downloaded from https://onlinelibrary.wiley.com/doi/10.1002/zamm.202300217 by University Of Witwatersrand, Wiley Online Library on [20/08/2024]. See the Terms and Conditions (https://onlinelibrary.wiley.com/terms-and-conditions) on Wiley Online Library for rules of use; OA articles are governed by the applicable Creative Commons License

TABLE 3 Convergence analysis of the spectral local linearization method (SLLM) with 50 collocation points using the following parameter values of $\Gamma_1 = 2.0, \beta = 0.01, \Omega = 1.0, Da = 10.0, \xi_0 = 2.5, \xi_1 = 0.98, \xi_2 = 1.0, R = 2.0, Pr = 21.0, Q = 0.0001, M = 2.0$ and $\phi = 0.02$.

Iterations	SLLM					
	$\xi = 1.0$			$\xi = -1.0$		
r	$f'''(0)$	$g''(0)$	$-\theta'(0)$	$f'''(0)$	$g''(0)$	$-\theta'(0)$
3.0	9.80390	7.62916	1.26485	−2.28983	−7.69140	0.03060
5.0	9.80388	7.62916	1.26484	−2.28985	−7.69141	0.03060
10.0	9.80388	7.62916	1.26484	−2.28990	−7.69141	0.03060
15.0	9.80388	7.62916	1.26484	−2.28988	−7.69141	0.03060

Abbreviation: SSLM, spectral local linearization method.

TABLE 4 Validation of $-f''(0)$ with variation of M when $\Gamma_1 = \beta = \Omega = 0.0, Da \to \infty, \xi_0 = 2.5, \xi_1 = 0.98, \xi_2 = 1.0, R = Pr = 0.0, Q = 0.0001, \xi = 1.0$ and $\phi = 0.00$.

	Lawal *et al.* [48]	Alsaedi *et al.* [52]	Current
M	$-f''(0)$		
0.0	1.00000	1.00000	1.000000
0.5	1.11803	1.11803	1.118033
1.0	1.41421	1.41421	1.414213

TABLE 5 Result comparison of $Re_x^{\frac{1}{2}} C_{fx}$, $Re_x^{\frac{1}{2}} C_{fy}$ and $Re_x^{-\frac{1}{2}} Nu_x$ of the present model with the work of Wang [34] in the absence of nanoparticles composition with $\beta = M = R = Q = \Gamma_1 = 0$ and $Da \to \infty$.

	Present results					Wang [34]				
Ω	$Re_x^{\frac{1}{2}} C_{fx}$	$Re_x^{\frac{1}{2}} C_{fy}$	$Re_x^{-\frac{1}{2}} Nu_x$ when Pr			$Re_x^{\frac{1}{2}} C_{fx}$	$Re_x^{\frac{1}{2}} C_{fy}$	$Re_x^{-\frac{1}{2}} Nu_x$ when Pr		
			0.7	2.0	7.0			0.7	2.0	7.0
0.0	1.00000	0.00000	0.453932	0.911358	1.89541	1.0000	0.0000	0.455	0.911	1.895
0.5	1.13838	0.51276	0.389353	0.852436	1.85118	1.1384	0.5128	0.390	0.853	1.850
1.0	1.32503	0.837098	0.322178	0.770299	1.78762	1.3250	0.8371	0.321	0.770	1.788
2.0	1.65235	1.28726	0.248103	0.63776	1.66436	1.6523	1.2873	0.242	0.638	1.664
5.0	2.39014	2.15053	0.172899	0.439197	1.36055	–	–	–	–	–

4.1 | Numerical validation

In this section, validation and accuracy of the SLLM using different metrics is reported. Convergence of the spectral method is displayed in Table 3 for Equations (13), (14) and (15), the method shows a speedy convergence by the tenth iterations. Validation of the spectral method is executed in Table 4 and Table 5. The numerical value of the temperature gradient and skin friction coefficient using the SLLM and for other previous results in literature are tabulated. The comparative results show good agreement with previously established results in the limiting cases. Thus, the numerical method (SLLM) is suitable to provide reasonable approximate solution to the system of ordinary differential equations given in Equations (13), (14) and (15) with its boundary conditions outlined in Equation (17).

5 | RESULTS AND DISCUSSION

In this section, we investigate the importance of each parameter and provide explanation as to the factors affecting the fluid flow and heat transfer of a Jeffrey nanofluid over a rotating contracting or expanding sheet with variable Darcy regime.

It is worth mentioning that only the nanofluid (blood + gold composition) heat and mass flow is given consideration. To carry out the computational simulation, the numerical value of $\Gamma_1 = 2.0, \beta = 0.01, \Omega = 1.0, Da = 10.0, \xi_0 = 2.5, \xi_1 = 0.98, \xi_2 = 1.0, R = 2.0, Pr = 21.0, Q = 0.0001, M = 2.0$ were used, unless otherwise stated. Figures 2 and 3 shows the influence of volume fraction nanoparticles ϕ on the primary velocity and secondary velocity profile for shrinking and stretching

15214001, 2024, 2, Downloaded from https://onlinelibrary.wiley.com/doi/10.1002/zamm.202300217 by University Of Witwatersrand, Wiley Online Library on [20/08/2024]. See the Terms and Conditions (https://onlinelibrary.wiley.com/terms-and-conditions) on Wiley Online Library for rules of use; OA articles are governed by the applicable Creative Commons License

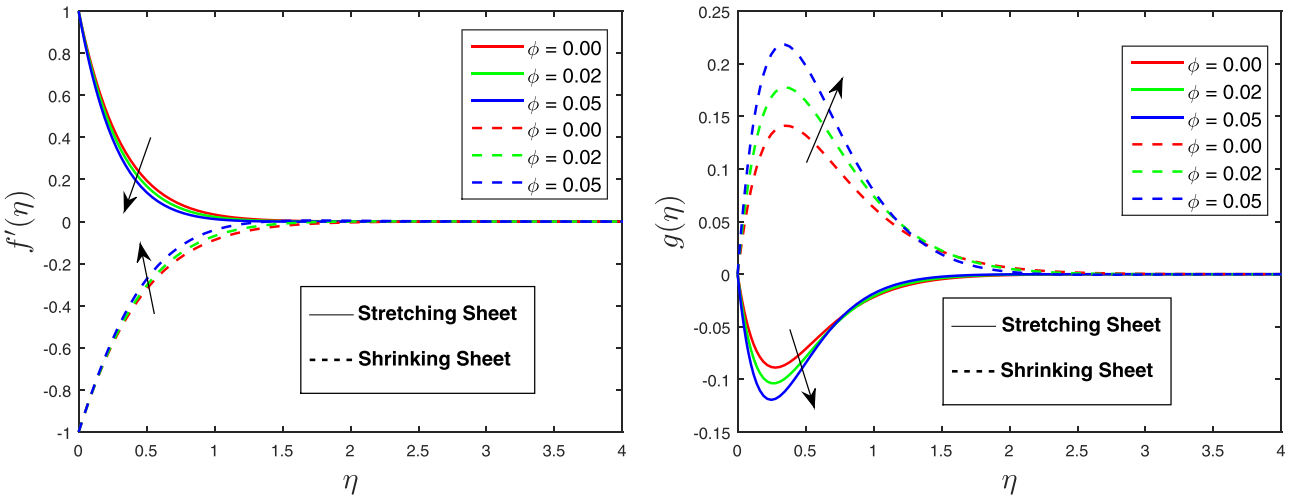


FIGURE 3 Variation of ϕ on the flow profiles against η.

sheets. With the introduction of nanoparticles volume fractions into the flow system, the primary velocity profile of the stretching sheet is downsized. However, a boost in the primary velocity profile is experienced for shrinking sheet. This may be attributed to the fact that injection of the nanoparticle into the stretching sheet reduced the shear force nature of the fluid. As more nanoparticle volume fractions are introduced into the contracting sheet, the shear force increases, thus increasing the velocity profile. The nanoparticle effect on the secondary velocity distribution has similar dynamics to the primary velocity profile in both the stretching and shrinking sheet. The rotational parameter Ω (Eckman number) influence is displayed in Figure 4. The Eckman number give attributes to the ratio of the viscous and Coriolis forces in the system. We observed that the magnitude of enhancement experienced in the shrinking sheet as we increase the Eckman number is relatively more than its negative impact that is, experienced in the stretching sheet for both velocity (primary and secondary) profiles. In this scenario, the mechanics is best explained as the viscous force decreases as the Coriolis force increases. This led to a reduction in the velocity profiles of the stretching sheet. However, there was a boost in the shrinking sheet due to the shear force contributed by the shrinking nature of the sheet.

The temperature distribution is diametrically opposed for the shrinking and stretching sheets. More heat is dissipated as the magnitude of the Eckman number increases in the stretching sheet but is downsized for the shrinking sheet. This occurrence is because as the fluid velocity drags slowly over the sheet, more heat is generated thus increasing the temperature distribution profile. A similar, but opposite explanation for the decrease in the shrinking sheet's temperature profile distribution has already been captured. The influence of the relaxation times to the retardation times ratio Γ_1 for the Jeffrey fluid is presented graphically in Figure 5. The magnitude of increase and decrease in the shrinking and stretching sheets are quite similar. Although the stretching sheet primary velocity profile seems to attain equilibrium at the far field when compared to its shrinking sheet primary velocity profile, in particular at $\Gamma_1 = 1.0$. In the secondary velocity, the flow in both sheets show different dynamics close to the wall and far away before coming to rest at the far field condition. This can be viewed as a flow separation area where fluid velocity decreases with increment in Γ_1 after initially experiencing reduction close to the boundary at $\eta = 0$ for the stretching sheet and vice-versa phenomenon for the shrinking sheet is experienced. The temperature profile dynamics in Figure 5 are well captured as a reduction in fluid flow will boost heat generation for the stretching sheet. However, it will give a reduction in the temperature profile for the shrinking sheet due to the free flow of the fluid in this instance. The influence of the Darcy parameter (Da) on the momentum and thermal boundary layers is shown in Figure 6.

The Darcy parameter which captured the porosity nature of both the shrinking and stretching sheets looks at the ratio of the viscous force to the particle diameter with stretching/shrinking sheet ratio. Increasing Da downplay the flow of the nanofluid in the stretching sheet but support the flow of the contracting sheet for the primary velocity. It explained why it is realistic to expect that being porous will decrease flow due to escape, however in shrinking sheets, the effect of the porous nature will have a minor effect when compared to stretching sheets. The thermal radiation R and Prandtl number Pr effect is conspicuously demonstrated in Figure 7 for both expanding and contracting sheets. It is discovered that increase in Pr decreases the temperature profile for the stretching sheet. The behavior is as a result of Pr being strongly dependent on thermal diffusivity of the nanofluid from the definition $Pr = \frac{(\rho c_p)_f \nu_f}{\kappa_f}$ meaning that larger Pr has frail thermal diffusivity.

15214001, 2024, 2, Downloaded from https://onlinelibrary.wiley.com/doi/10.1002/zamm.202300217 by University Of Witwatersrand, Wiley Online Library on [20/08/2024]. See the Terms and Conditions (https://onlinelibrary.wiley.com/terms-and-conditions) on Wiley Online Library for rules of use; OA articles are governed by the applicable Creative Commons License

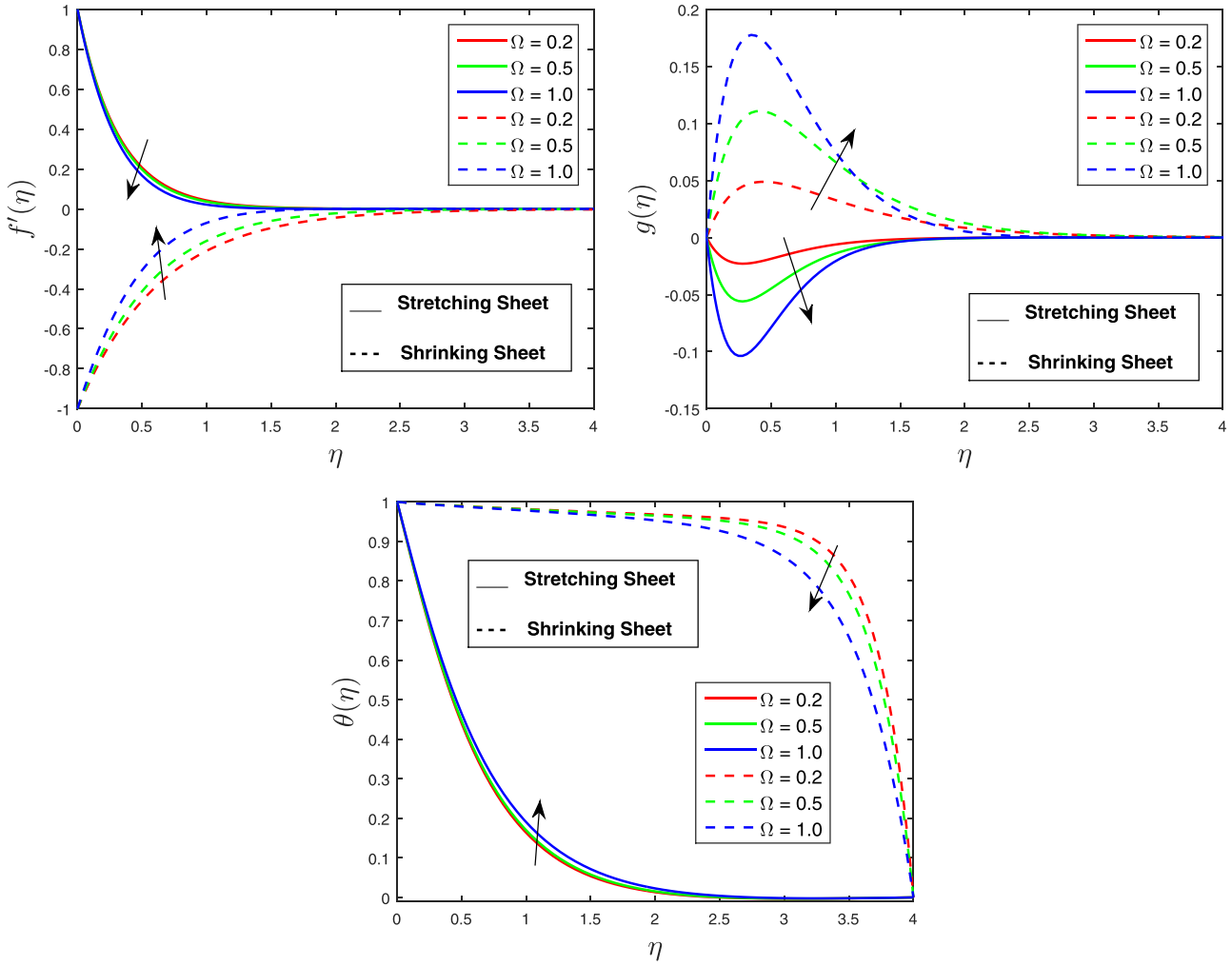


FIGURE 4 Variation of Ω on the flow profiles against η.

The behavior of the shrinking sheet for increase in Prandtl number is not far-fetched. This is simply due to the fact that stretching and shrinking sheet can be adjudged to exhibit opposite dynamics. The viscous force of the fluid is enhanced as the sheet contracts hence leading to more heat transfer in the shrinking sheet. It is observed from Figure 7 that an increase in the thermal radiation parameter R caused an increase in the temperature profile distribution for the stretching sheet. This is because the thermal radiation term provides an additional mechanism for heat transfer in a system. The result here agrees with the findings of Lawal *et al.* [48] A decrease in the temperature profile is observed for the shrinking sheet.

Figure 8 shows the importance of porous particle diameter on the velocity profiles. It can be adjudged that the impact of ξ_1 is more pronounced on the shrinking sheet compared to the stretching sheet. For the secondary velocity $g(\eta)$, as the porous particle diameter widen, fluid flowing in the shrinking sheet experience more drag before coming to rest at the far field. In the stretching sheet, increasing xi_1 downsize the velocity of the fluid.

5.1 | Discussion of the engineering physical quantity

Table 6 shows the engineering physical quantities (skin frictions and Nusselt number) for the base fluid at $\xi = 1$, nanofluid flow over a stretching sheet and nanofluid flow over a contracting sheet. For the stretching sheet flow, the skin drag force in the primary and secondary case is higher in the base fluid only when compared to the nanofluid (base fluid + gold particles) composition. For instance, considering $\Omega = 1.0$, the skin drag force reduces by 36% for the primary skin drag force and 57% for the secondary skin drag force. In a diametrically opposed version to the skin coefficient, the Nusselt number in the nanofluid composition is higher compared to the base fluid in all instances. In the scenario of $M = 1$, the Nusselt number increases by 2% from the base fluid to the nanofluid. This implies that the nanoparticle enhanced the

15214001, 2024, 2, Downloaded from https://onlinelibrary.wiley.com/doi/10.1002/zamm.202300217 by University Of Witwatersrand, Wiley Online Library on [20/08/2024]. See the Terms and Conditions (https://onlinelibrary.wiley.com/terms-and-conditions) on Wiley Online Library for rules of use; OA articles are governed by the applicable Creative Commons License

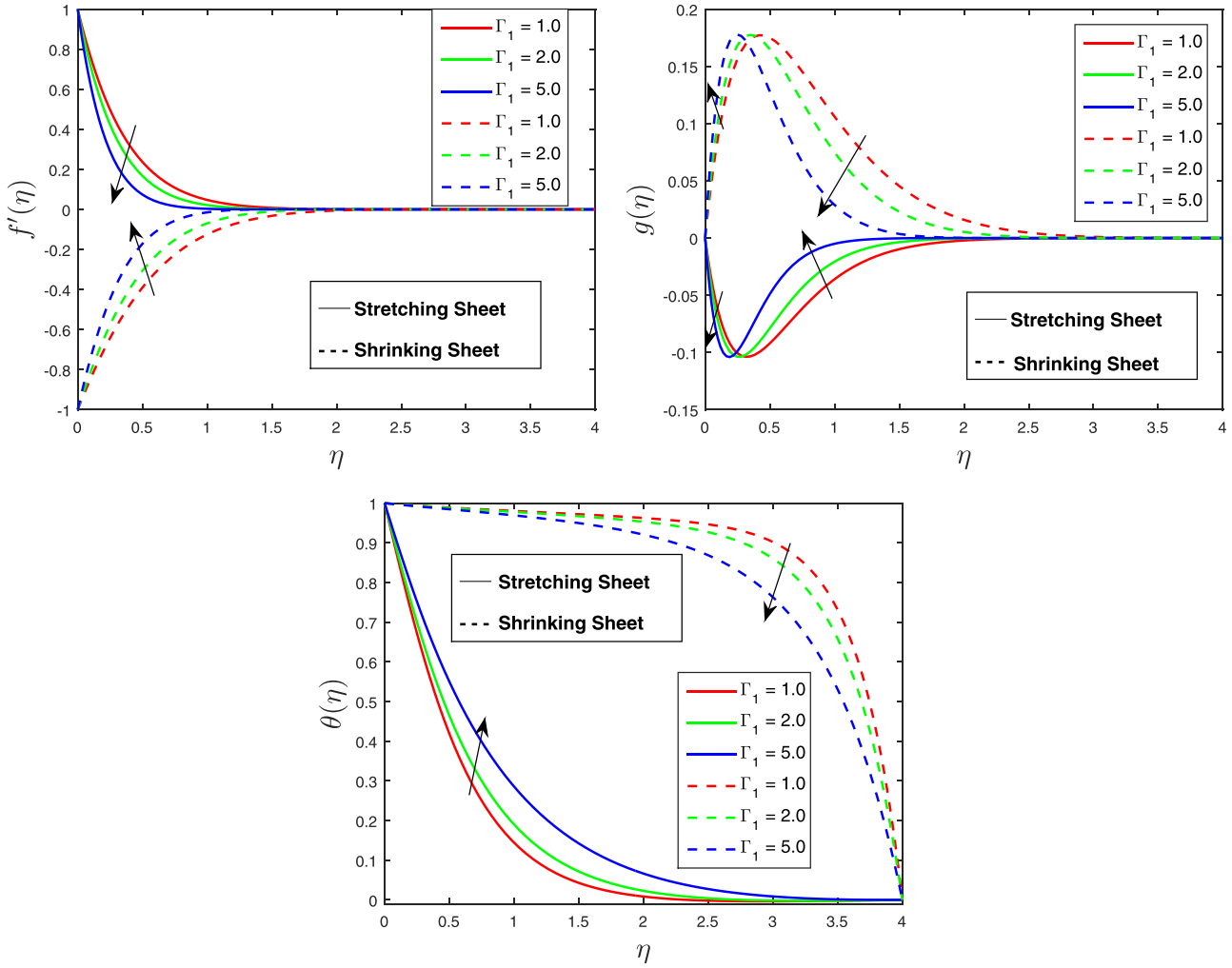


FIGURE 5 Variation of Γ_1 on the flow profiles against η.

heat transfer rate of the base fluid. It is clearly seen from Table 6 that the skin coefficient for the stretching sheet is far less than that of the shrinking sheet. If we consider the Nusselt number of the base fluid in the stretching sheet to that of the shrinking sheet for nanofluid, we observed that the nanofluid suppresses the heat transfer ratio of the base fluid.

6 | CONCLUSION

Numerical analysis on the investigation of surface dynamics (shrinking or stretching), thermophysical properties, Darcy law, Coriolis force, and heat transfer through radiation and heat source for the flow of a Jeffrey nanofluid (blood + gold particles) over a moving surface is conducted. In comparison with the second grade and viscous fluids, Jeffrey fluid rheology encompasses more distinct features considering it ability to predict the fluid retardation time paradox. As such, its application in cooling, casting, fermented, and transport systems are enormous. The transformation approach, numerical procedure and the new finding ascertain the achievement of the set goal. Upon suitable transformation, the dimensional governing differential equation is systematically neutralized into a dimensionless ordinary differential equation. Insight into the flow profiles is obtained using the SLLM. The presented numerical results have been shown to agree with the model's physics. Additionally, the numerical method has been benchmarked against previously published results in some limited cases. Some of the major findings of this study include the following:

1. The nanofluid movement and heat transfer of the stretching and shrinking sheets are diametrically opposed in all instances.

15214001, 2024, 2, Downloaded from https://onlinelibrary.wiley.com/doi/10.1002/zamm.202300217 by University Of Witwatersrand, Wiley Online Library on [20/08/2024]. See the Terms and Conditions (https://onlinelibrary.wiley.com/terms-and-conditions) on Wiley Online Library for rules of use; OA articles are governed by the applicable Creative Commons License

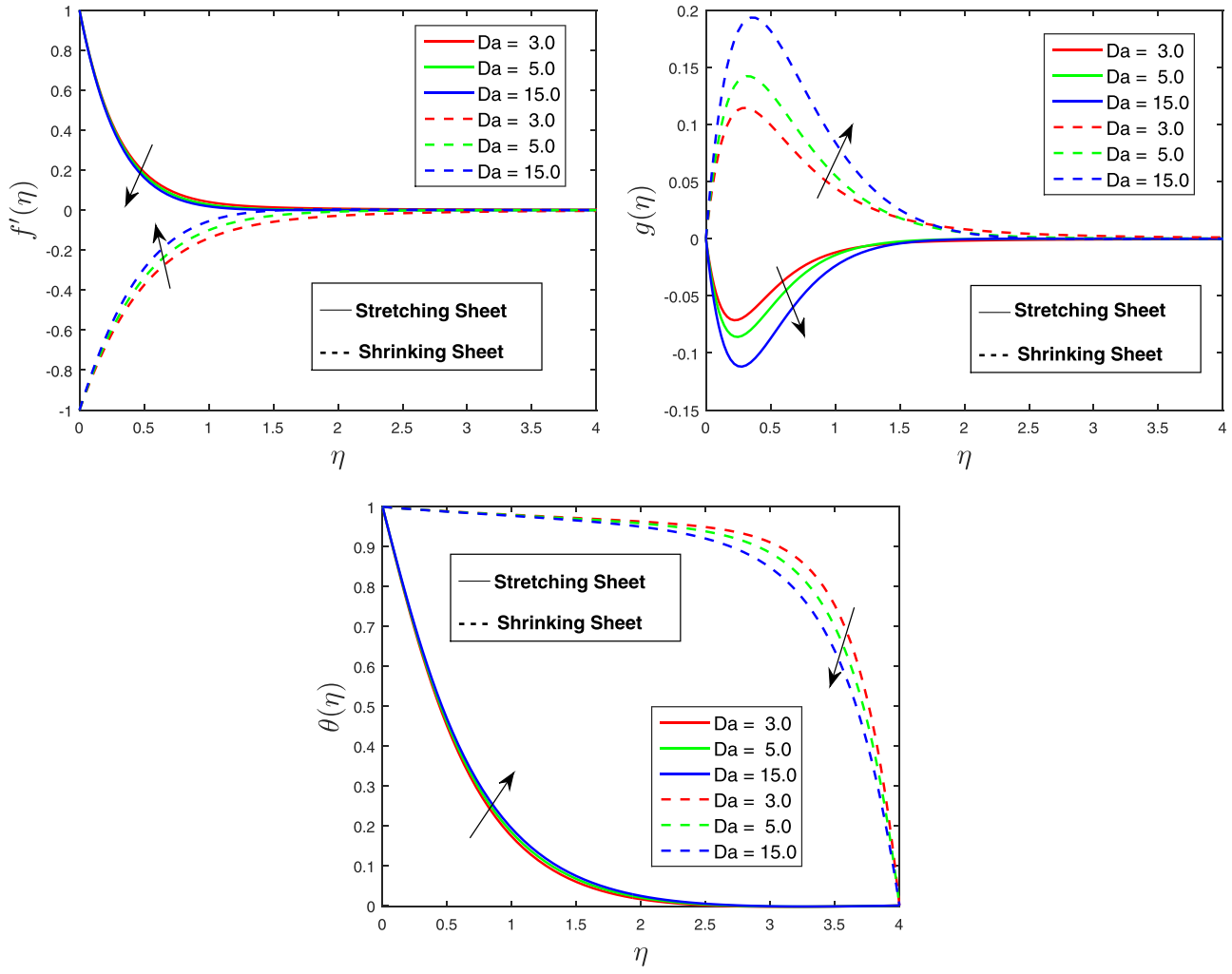


FIGURE 6 Variation of Da on the flow profiles against η.

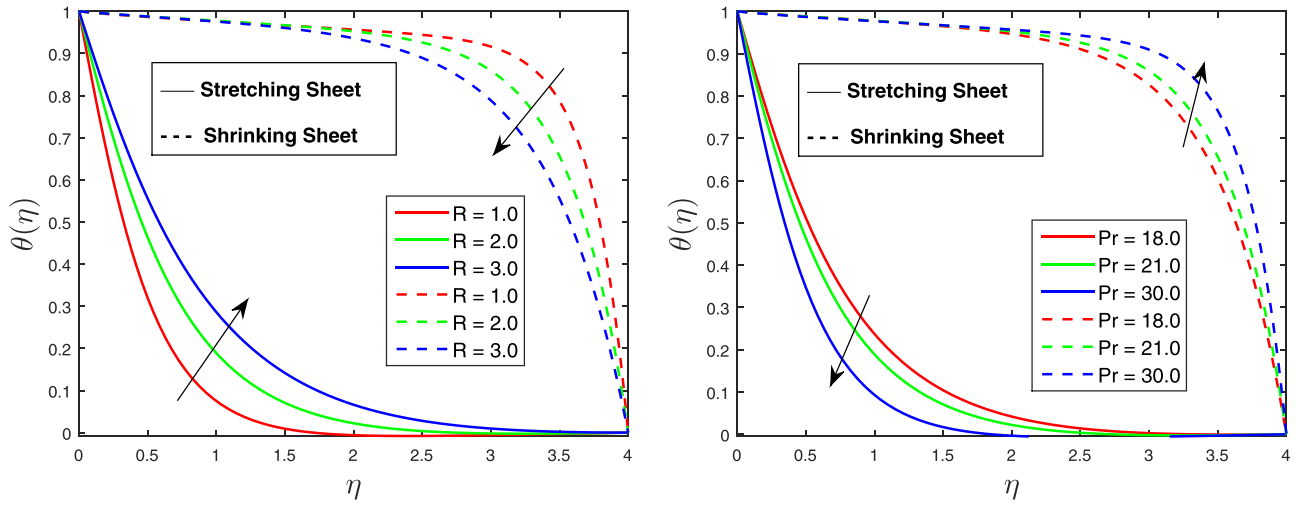


FIGURE 7 Variation of R and Pr on the temperature profile against η.

15214001, 2024, 2, Downloaded from https://onlinelibrary.wiley.com/doi/10.1002/zamm.202300217 by University Of Witwatersrand, Wiley Online Library on [20/08/2024]. See the Terms and Conditions (https://onlinelibrary.wiley.com/terms-and-conditions) on Wiley Online Library for rules of use; OA articles are governed by the applicable Creative Commons License

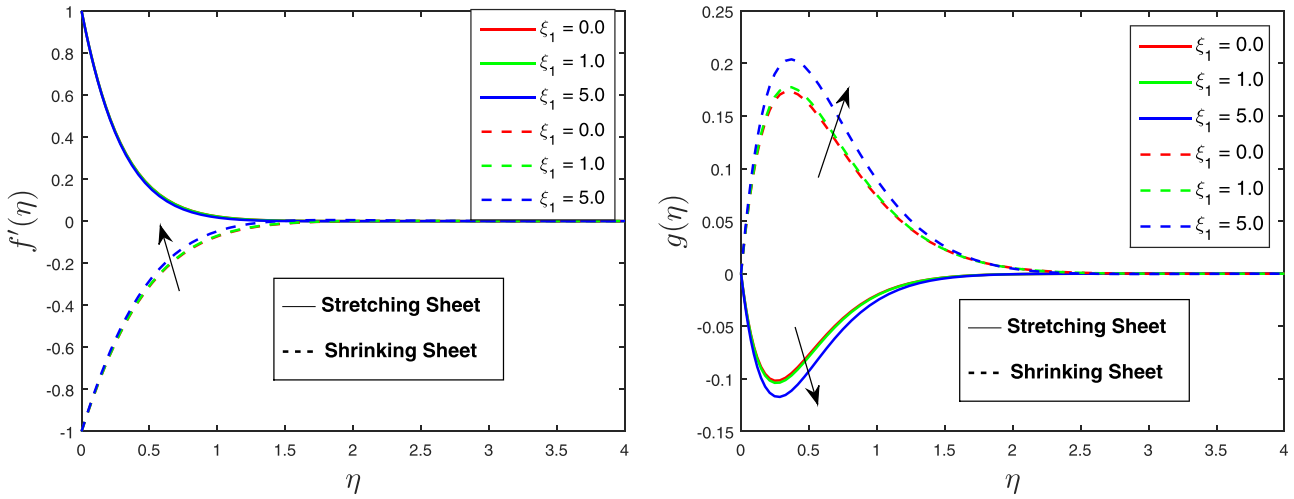


FIGURE 8 Variation of ξ_1 on the velocity profile against η.

TABLE 6 Computation results of $Re_x^{\frac{1}{2}}C_{fx}$, $Re_x^{\frac{1}{2}}C_{fy}$ and $Re_x^{-\frac{1}{2}}Nu_x$ for blood base fluid and when nanoparticles are injected with different values of model contributing parameters with thermophysical parameters in Table 1.

Values		Base fluid $\xi = 1$			*Au*+ Blood nanofluid $\xi = 1$			*Au*+ Blood nanofluid $\xi = -1$		
		$Re_x^{\frac{1}{2}}C_{fx}$	$Re_x^{\frac{1}{2}}C_{fy}$	$Re_x^{-\frac{1}{2}}Nu_x$	$Re_x^{\frac{1}{2}}C_{fx}$	$Re_x^{\frac{1}{2}}C_{fy}$	$Re_x^{-\frac{1}{2}}Nu_x$	$Re_x^{\frac{1}{2}}C_{fx}$	$Re_x^{\frac{1}{2}}C_{fy}$	$Re_x^{-\frac{1}{2}}Nu_x$
Ω	1.0	−1.04768	−0.28614	4.68511	−1.42289	−0.44790	4.80885	0.84767	0.58090	0.11657
	2.0	−1.14317	−0.53237	4.31426	−1.58430	−0.81661	4.31446	1.14277	0.96845	0.13139
	3.0	−1.25654	−0.73593	3.89808	−1.76140	−1.11872	3.89964	1.34642	1.33958	0.12949
β	0.00	−1.04257	−0.28707	4.67443	−1.41599	−0.44935	4.79714	0.85167	0.57917	0.11644
	0.01	−1.04795	−0.28603	4.68259	−1.42296	−0.44786	4.80832	0.84774	0.58087	0.11657
	0.02	−1.05304	−0.28512	4.69317	−1.42983	−0.44643	4.81989	0.84371	0.58260	0.11670
D_a	5.0	−1.03496	−0.25879	4.77385	−1.40530	−0.40766	4.90349	0.80177	0.51818	0.11522
	10.0	−1.04794	−0.28604	4.68272	−1.42296	−0.44787	4.80834	0.84772	0.58087	0.11657
	15.0	−1.05128	−0.29871	4.66282	−1.42868	−0.46588	4.78117	0.86456	0.60934	0.11726
Γ_1	1.0	−1.28313	−0.35026	5.09199	−1.74257	−0.54833	5.25514	1.03783	0.71109	0.11202
	2.0	−1.04793	−0.28604	4.68276	−1.42295	−0.44787	4.80835	0.84772	0.58087	0.11657
	3.0	−0.90757	−0.24779	4.36770	−1.23237	−0.38796	4.46739	0.73430	0.50320	0.12096
M	1.0	−0.88699	−0.32606	4.97257	−1.23565	−0.50272	5.05585	0.56287	0.70778	0.11011
	2.0	−1.04795	−0.28604	4.68264	−1.42296	−0.44786	4.80832	0.84774	0.58087	0.11657
	3.0	−1.19094	−0.25732	4.43755	−1.59412	−0.40650	4.58688	1.08784	0.49987	0.12264

2. As a result of the Eckman number upsurge, primary and secondary velocities are dampened in the stretching sheet, but heat distribution is enhanced in this scenario.
3. The nanoparticles improves the heat transfer rate of the base fluid. For examples, the Nusselt number increases from 4.68511 to 4.80885 when $\Omega = 1$ for the stretched surface.
4. A blood sample containing gold particles is advised for lesser drag force in the stretching sheet but greater drag force in the shrinking sheet compared to a blood sample (stretching sheet) only in both situations.
5. The impact of the porous particle diameter is more pronounced in the shrinking sheet compared to the stretching sheet.
6. The variable Darcy parameter downsizes momentum response in stretching case while these velocities magnify for shrinking instance.

Using the results of this study, researchers will be able to understand better the effect of gold nanoparticles in rotating systems and the heating phenomenon. Additionally, it helps in photo-catalysis, x-ray imaging, computed tomography (CT),

15214001, 2024, 2, Downloaded from https://onlinelibrary.wiley.com/doi/10.1002/zamm.202300217 by University Of Witwatersrand, Wiley Online Library on [20/08/2024]. See the Terms and Conditions (https://onlinelibrary.wiley.com/terms-and-conditions) on Wiley Online Library for rules of use; OA articles are governed by the applicable Creative Commons License

radiation therapy (RT), diagnosis, and other biological activities. Blood centrifugation is another practical application of the present study. We plan to investigate the stability of flow (existence of dual/multiple solutions) and heat characteristics by utilizing a hybrid nanofluid composition in our future study. The objective of the research is to determine whether the use of hybrid nanoparticles can enhance the heat transfer of the fluid, while taking into account the same flow formation and environmental factors.

ACKNOWLEDGMENTS

The authors have nothing to report.

ORCID

Yusuf O. Tijani https://orcid.org/0000-0002-9127-7173
Mojeed T. Akolade https://orcid.org/0000-0002-6876-7203
Olumuyiwa Otegbeye https://orcid.org/0000-0003-1321-9776
Abdulhakeem Yusuf https://orcid.org/0000-0001-8675-5137

REFERENCES

[1] Child, P.R.N.: Rotating flows. Butterworth-Heinemann, vol. 1, pp. 1–389. Elsevier, Oxford (UK) (2011)
[2] Tokis, J.N.: Unsteady magnetohydrodynamic free-convection flows in a rotating fluid. Astrophys. Space Sci. 119, 305–313 (1986)
[3] Nanousis, N.D.: Unsteady magnetohydrodynamic flows in a rotating elasto-viscous fluid. Astrophys. Space Sci. 199, 317–321 (1993)
[4] Abbas, Z., Javed, T., Sajid, M., Ali, N.: Unsteady MHD flow and heat transfer on a stretching sheet in a rotating fluid. J. Taiwan Inst. Chem. Eng. 41(6), 644–650 (2010)
[5] Shafique, Z., Mustafa, M., Mushtaq, A.: Boundary layer flow of Maxwell fluid in rotating frame with binary chemical reaction and activation energy. Results Phys. 6, 627–633 (2016)
[6] Saleem, S., Rafiq, H., Alqahtani, A.S., El-Aziz, M.E.A., Malik, M.Y., Animasaun, I.L.: Magneto Jeffrey nanofluid bioconvection over a rotating vertical cone due to Gyrotactic microorganism. Math. Probl. Eng. 1–11 (2019)
[7] Narayana, P.V.S., Tarakaramu, N., Sarojamma, G., Animasaun, I.L.: Numerical simulation of nonlinear thermal radiation on the 3D flow of a couple stress Casson nanofluid due to a stretching sheet. J. Therm. Sci. Eng. Appl. 13, (2021)
[8] Naidu, K.K., Babu, D.H., Reddy, S.H., Narayana, P.V.S.: Radiation and partial slip effects on magnetohydrodynamic Jeffrey nanofluid containing Gyrotactic microorganisms over a stretching surface. J. Therm. Sci. Eng. Appl. 13, 1–28 (2020)
[9] Pötschke, P., Fornes, T.D., Paul, D.R.: Rheological behavior of multiwalled carbon nanotube/polycarbonate composites. Polymer 43, 3247–3255 (2002)
[10] Phuoc, T.X., Massoudi, M., Chen, R.-H.: Viscosity and thermal conductivity of nanofluids containing multi-walled carbon nanotubes stabilized by chitosan. Int. J. Therm. Sci. 50, 12–18 (2011)
[11] Hayat, T., Rafiq, M., Ahmad, B.: Soret and Dufour effects on MHD peristaltic flow of Jeffrey fluid in a rotating system with porous medium. PLoS ONE 11, e0145525 (2016)
[12] Rao, A.S., Nagendra, N., Ramachandra Prasad, V.: Heat transfer in a non-Newtonian Jeffrey's fluid over a non-isothermal wedge. Procedia Eng. 127, 775–782 (2015)
[13] Hayat, T., Aziz, A., Muhammad, T., Alsaedi, A.: A revised model for Jeffrey nanofluid subject to convective condition and heat generation/absorption. PLoS ONE 12, e0172518 (2017)
[14] Hussain, T., Shehzad, S.A., Hayat, T., Alsaedi, A., Al-Solamy, F.R., Ramzan, M.: Radiative hydromagnetic flow of Jeffrey nanofluid by an exponentially stretching sheet. PLoS ONE 9, e103719 (2014)
[15] Hayat, T., Mustafa, M.: Influence of thermal radiation on the unsteady mixed convection flow of a Jeffrey fluid over a stretching sheet. Z. Naturforsch. A 65, 711–719 (2010)
[16] Idowu, A.S., Jimoh, A., Ahmed, L.S.: Impact of heat and mass transfer on MHD oscillatory flow of Jeffrey fluid in a porous channel with thermal conductivity, Dufour and Soret. J. Appl. SCI. Environ. Manag. 19, 819–830 (2016)
[17] Zin, N.A.M., Khan, I., Shafie, S.: Influence of thermal radiation on unsteady MHD free convection flow of Jeffrey fluid over a vertical plate with ramped wall temperature. Math. Probl. Eng. 2016, 1–12 (2016)
[18] Zeeshan, A., Majeed, A.: Heat transfer analysis of Jeffrey fluid flow over a stretching sheet with suction/injection and magnetic dipole effect. Alex. Eng. J. 55, 2171–2181 (2016)
[19] Gaffar, S.A., Prasad, V.R., Reddy, E.K.: Computational study of Jeffrey's non-Newtonian fluid past a semi-infinite vertical plate with thermal radiation and heat generation/absorption. Ain Shams Eng. J. 8, 277–294 (2017)
[20] Kothandapani, M., Prakash, J.: Convective boundary conditions effect on peristaltic flow of a MHD Jeffrey nanofluid. Appl. Nanosci. 6, 323–335 (2016)
[21] Bhatti, M.M., Zeeshan, A.: Analytic study of heat transfer with variable viscosity on solid particle motion in dusty Jeffrey fluid. Mod. Phys. Lett. B 30, 1650196 (2016)
[22] Li, S., khan, M.I., Alzahrani, F., Eldin, S.M.: Heat and mass transport analysis in radiative time dependent flow in the presence of Ohmic heating and chemical reaction, viscous dissipation: an entropy modeling. Case Stud. Therm. Eng. 42, 102722 (2023)
[23] Hayat, T., Shafiq, A., Alsaedi, A.: MHD axisymmetric flow of third grade fluid by a stretching cylinder. Alex. Eng. J. 54(2), 205–212 (2015)

15214001, 2024, 2, Downloaded from https://onlinelibrary.wiley.com/doi/10.1002/zamm.202300217 by University Of Witwatersrand, Wiley Online Library on [20/08/2024]. See the Terms and Conditions (https://onlinelibrary.wiley.com/terms-and-conditions) on Wiley Online Library for rules of use; OA articles are governed by the applicable Creative Commons License

[24] Hayat, T., Shafiq, A., Nawaz, M., Alsaedi, A.: MHD axisymmetric flow of third grade fluid between porous disks with heat transfer. Appl. Math. Mech. 1, 749–764 (2012)
[25] Shafiq, A., Rasool, G., Khalique, C.M., Aslam, S.: Second grade bioconvective nanofluid flow with buoyancy effect and chemical reaction. Symmetry 12(4), 621 (2020)
[26] Liu, Z., Li, S., Sadaf, T., Khan, S.U., Alzahrani, F., Khan, M.I., Eldin, S.M.: Numerical bio-convective assessment for rate type nanofluid influenced by Nield thermal constraints and distinct slip features. Case Stud. Therm. Eng. 44, 102821 (2023)
[27] Hamid, A., Hashim, Khan, M., Hafeez, A.: Unsteady stagnation-point flow of Williamson fluid generated by stretching/shrinking sheet with Ohmic heating. Int. J. Heat Mass Transf. 126, 933–940 (2018)
[28] Yasin, M.H.M., Ishak, A., Pop, I.: MHD heat and mass transfer flow over a permeable stretching/shrinking sheet with radiation effect. J. Magn. Magn. Mater. 407, 235–240 (2016)
[29] Gangadhar, K., Kannan, T., Jayalakshmi, P.: Magnetohydrodynamic micropolar nanofluid past a permeable stretching/shrinking sheet with Newtonian heating. J. Braz. Soc. Mech. Sci. Eng. 39, 4379–4391 (2017)
[30] Seini, I.Y., Makinde, D.O.: Boundary layer flow near stagnation-points on a vertical surface with slip in the presence of transverse magnetic field. Int. J. Numer. Methods Heat Fluid Flow 24, 643–653 (2014)
[31] Aleem, M., Asjad, M.I., Ahmadian, A., Salimi, M., Ferrara, M.: Heat transfer analysis of channel flow of MHD Jeffrey fluid subject to generalized boundary conditions. Eur. Phys. J. Plus 135, 26 (2020)
[32] Motsa, S.S.: A new spectral local linearization method for nonlinear boundary layer flow problems. J. Appl. Math. 2013, (2013)
[33] Iqbal, Z., Sajid, M., Hayat, T., Obaidat, S.: Flow and heat transfer with prescribed skin friction in a rotating fluid. Int. J. Numer. Methods Fluids (68), 872–886 (2011)
[34] Wang, C.Y.: Stretching a surface in a rotating fluid. J. Appl. Math. Phys. (39), 1–9 (1988)
[35] Akolade, M.T., Tijani, Y.O.: A comparative study of three dimensional flow of Casson–Williamson nanofluids past a riga plate: spectral quasi-linearization approach. Partial Differ. Equ. Appl. 4, 100108 (2021)
[36] Nithiarasu, P., Seetharamu, K.N., Sundararajan, T.: Natural convective heat transfer in a fluid saturated variable porosity medium. Int. J. Heat Mass Transf. 40(16), 3955–3967 (1997)
[37] Tlau, L., Ontela, S.: Entropy analysis of hybrid nanofluid flow in a porous medium with variable permeability considering isothermal/isoflux conditions. Chin. J. Phys. 80, 239–252 (2022)
[38] Chamkha, A.J., Issa, C., Khanafer, K.: Natural convection from an inclined plate embedded in a variable porosity porous medium due to solar radiation. Int. J. Therm. Sci. 41(1), 73–81 (2002)
[39] Santos-Moreno, M., Valencia-Negrete, C.V., Fernández-Anaya, G.: Conformable derivatives in viscous flow describing fluid through porous medium with variable permeability. Fractals 2250178 (2022)
[40] Zakharovl, M., Sadovsky, M.: The role of blood circulatory system in thermal regulation of animals explained by entropy production analysis. (2013)
[41] Vogel, E.E., Belmar, N., Stockins, B.: Possible effects of oriented magnetic fields on human blood pressure. Int. J. Cardiol. Sci. 35(6), 697–705 (2022)
[42] Jamshed, W., Devi, S.U., Goodarzi, M., Prakash, M., Nisar, K.S., Zakarya, M., Abdel-Aty, A.: Evaluating the unsteady Casson nanofluid over a stretching sheet with solar thermal radiation: an optimal case study. Case Stud. Therm. Eng. 26, 101160 (2021)
[43] Sheikholeslami, M., Hatami, M., Ganji, D.D.: Nanofluid flow and heat transfer in a rotating system in the presence of a magnetic field. J. Mol. Liq. 190, 112–120 (2014)
[44] Arunachalam, M., Rajappa, N.R.: Forced convection in liquid metals with variable thermal conductivity and capacity. Acta Mech. (31), 305–309 (1978)
[45] Nuwairan, M.A., Souayeh, B.: Simulation of gold nanoparticle transport during MHD electroosmotic flow in a peristaltic micro-channel for biomedical treatment. Micromachines 13, 374 (2022)
[46] Motsa, S.S.: A new spectral local linearization method for nonlinear boundary layer flow problems. J. Appl. Math. 013, 423628 (2013)
[47] Otegbeye, O., Goqo, S.P., Ansari, Md.S.: Comparative study of some spectral based methods for solving boundary layer flow problems. AIP Conf. Proc. 2253, 020013 (2020)
[48] Lawal, M.O., Kasali, K.B., Ogunseye, H.A., Oni, M.O., Tijani, Y.O., Lawal, Y.T.: On the mathematical model of Eyring-Powell nanofluid flow with non-linear radiation, variable thermal conductivity and viscosity. Partial Differ. Equ. Appl. 5, 100318 (2022)
[49] Ogunseye, H.A., Mondal, H., Sibandai, P.: Lie group analysis of a Powell–Eyring nanofluid flow over a stretching surface with variable properties. SN Appl. Sci. 2(115), 1–15 (2020)
[50] Oloniiju, S.D., Oyelakin, I.S., Goqo, S.P., Sibanda, P.: Numerical and machine learning analyses of entropy generation in an unsteady squeezing flow of copper/aluminum oxide/water hybrid nanofluid. Heat Transf. 50(4), 3822–3841 (2021)
[51] Trefethen, L.N.: Spectral Methods in MATLAB. SIAM, New York (2000)
[52] Alsaedi, A., Khan, M.I., Farooq, M., Gull, N., Hayat, T.: Magnetohydrodynamic (MHD) stratified bioconvective flow of nanofluid due to gyrotactic microorganisms. Adv. Powder Technol. 28(1), 288–298 (2017)

How to cite this article: Tijani, Y.O., Akolade, M.T., Otegbeye, O., Yusuf, A.: Surface dynamics on Jeffrey nanofluid flow with Coriolis effect and variable Darcy regime. Z Angew Math Mech. 104, e202300217 (2024). https://doi.org/10.1002/zamm.202300217

15214001, 2024, 2, Downloaded from https://onlinelibrary.wiley.com/doi/10.1002/zamm.202300217 by University Of Witwatersrand, Wiley Online Library on [20/08/2024]. See the Terms and Conditions (https://onlinelibrary.wiley.com/terms-and-conditions) on Wiley Online Library for rules of use; OA articles are governed by the applicable Creative Commons License